Journal of
Materials Chemistry A

PAPER

View Article Online
View Journal | View Issue

Cite this: J. Mater. Chem. A, 2015, 3, 2353

A homogeneous intergrown material of $LiMn_2O_4$ and $LiNi_{0.5}Mn_{1.5}O_4$ as a cathode material for lithium-ion batteries†

Jing Wang, Yang-yang Yu, Bi-he Wu, Wei-qing Lin, Ji-yang Li and Jin-bao Zhao*

Micro-/nano-structured spherical intergrown $LiMn_2O_4$–$LiNi_{0.5}Mn_{1.5}O_4$ (LMO–LNMO I, $LiNi_{0.25}Mn_{1.75}O_4$) particles as a cathode material have been synthesized by an impregnation method with highly reactive chestnut-like MnO_2 nano-spheres as a manganese source and structural template. The LMO–LNMO I consisted of aggregates of nano-sized particles with a well-defined cubic spinel structure. The electrochemical performance and thermostability of LMO–LNMO I are better than those of a simple mechanical mixture of $LiMn_2O_4$ and $LiNi_{0.5}Mn_{1.5}O_4$ (LMO–LNMO M), and much better than those of individual $LiMn_2O_4$ and $LiNi_{0.5}Mn_{1.5}O_4$ monomers. Within this special structure, LNMO acts as a skeleton to stabilize the structure of LMO and enables more lithium ions in LMO to participate in the charge–discharge process along with those in LNMO, leading to high specific discharge capacities. In addition, this material exhibits excellent cycle stabilities at room temperature (25 °C) as well as at elevated temperature. It presented a discharge capacity of 130 mA h g^{-1}, with 96.2% capacity retention after 100 cycles at 25 °C at 1 C. When the temperature and rate are increased to 55 °C and 5 C, it still delivers a discharge capacity of 131 mA h g^{-1}, with a capacity retention of 95% after 100 cycles. Being synthesized by a special impregnation method, LMO–LNMO I shows a more homogeneous ion mixing of Ni and Mn in the structure at the atomic level with a more enhanced thermostability due to its high Mn content compared to LNMO. The structural stability and high electrical conductivity of LMO–LNMO I are responsible for the excellent electrochemical performance and outstanding thermal stability.

Received 6th October 2014
Accepted 3rd December 2014

DOI: 10.1039/c4ta05311g

www.rsc.org/MaterialsA

1. Introduction

The launch of environmentally benign electric vehicles (EVs), hybrid electric vehicles (HEVs) and plug-in hybrid electric vehicles (PHEVs) has accelerated rapid developments in the power battery technology and market.[1–5] As a new generation of high-energy batteries, lithium ion batteries have many advantages such as high voltage, high specific capacity, excellent cycling performance, and so on.[6,7] They are widely considered as the main power source for transportation vehicles in the future.[8,9] Due to its low cost, low toxicity and good safety performance, the spinel $LiMn_2O_4$ (LMO) material is considered to be an ideal cathode material for batteries.[10–12] Compared with two-dimensional layered cubic rock-salt $LiCoO_2$,[13] a standard cathode material used in electronic device batteries whose structure undergoes undesirable changes that degrade its electrochemical performance,[14] especially in an overcharged state, spinel $LiMn_2O_4$ is a true three-dimensional material with channels capable of fast transportation of lithium ions with relatively stable thermodynamics and preservation of its structure.[14,15] However the $LiMn_2O_4$ material has a major disadvantage, *i.e.*, the fast fading of capacity, which is attributed to the following intrinsic chemistries: (1) Jahn–Teller effect.[16,17] During the charge and discharge process, especially at the deep depth of lithiation, spinel phase $LiMn_2O_4$ is readily transformed into tetragonal phase $Li_2Mn_2O_4$.[11,18] With the contraction and expansion of the structural building block of the MnO_6 octahedron, the spinel structure is destroyed. The structural change causes high electrical resistance, eventually resulting in the decline of electrochemical performance of the material. To maintain its structural integrity and cycle life, its capacity has to be sacrificed, *i.e.*, the material cannot be fully intercalated/deintercalated, which restricts its discharge capacity to about 110 mA h g^{-1}. (2) The dissolution of manganese into the electrolyte. Mn^{3+} ions are prone to the disproportionation reaction:[19]

$$2Mn^{3+} = Mn^{4+} + Mn^{2+} \tag{1}$$

The resulting Mn^{2+} ion is soluble in the electrolyte and can even be electrochemically deposited on the anode,[20] resulting in

---

State Key Lab of Physical Chemistry of Solid Surfaces, Collaborative Innovation Center of Chemistry for Energy Materials, College of Chemistry and Chemical Engineering, Xiamen University, Xiamen, Fujian, 361005, China. E-mail: jbzhao@xmu.edu.cn; Fax: +86-592-2186935; Tel: +86-592-2186935

† Electronic supplementary information (ESI) available. See DOI: 10.1039/c4ta05311g

a significant loss of active substances and capacity during cycling. Structural doping with other metal ions, such as Ni,[21] Co,[22] Al,[23] and Ti,[24] was proved to be beneficial for improving the LMO spinel structural and thermal stability.

Herein we report our synthesis and electrochemical study of intergrown $LiMn_2O_4$–$LiNi_{0.5}Mn_{1.5}O_4$ (LMO–LNMO I) particles, which are micron-sized spheres consisting of aggregated nanosized octahedral particles with a well-defined cubic spinel structure. In comparison, we have also synthesized spherical LMO and LNMO, and a mechanical mixture of them. The LMO–LNMO I material exhibits several features as cathode materials: firstly, it showed an excellent rate capability with specific discharge capacities of 123, 126.5, 128.2, 127, 124 and 122 mA h g^{-1} at 0.2 C, 0.5 C, 1 C, 2 C, 5 C and 10 C, respectively. Secondly, LNMO stabilizes the structure of LMO and is also an active material of high discharge plateau at 4.7 V,[25] consequently enhancing the specific energy of the composite materials compared to LMO. Thirdly, with the optimization of the Mn content in LMO–LNMO I, its thermo-stability is enhanced compared to LNMO.

2. Experimental

2.1. Material preparation

The nanoscale chestnut-cupule-like MnO_2 spheres (MnO_2–S) were prepared by a solvothermal method modified from the literature.[26] An aqueous solution of 20 mmol $MnSO_4$ was mixed with 8 ml of concentrated sulfuric acid, then $K_2S_2O_8$ solution was quickly poured into the solution under rapid stirring. The solution was kept in a water bath at 65 °C undisturbed for 18 h. After filtration and washing with deionized water and ethanol, the product was dried in an oven at 100 °C. The standard synthetic procedures of LNMO, LMO and LMO–LNMO intergrowth (LMO–LNMO I, molar ratio of LNMO/LMO, 1/1) are as follows.[27] In a typical synthesis of LNMO, 15 mmol of MnO_2–S, 5 mmol of $Ni(NO_3)_2\cdot 6H_2O$, and 10.8 mmol of $LiNO_3$ were dispersed into 20 ml ethanol. After being ground in a mortar for 30 minutes, the solution was evaporated slowly at 80 °C under constant stirring. The obtained precursor was firstly sintered in air at 800 °C for 20 h, then cooled down to 600 °C, and was maintained at this temperature for 20 h to compensate for oxygen vacancies with pyrolysis of the sample before cooling to room temperature slowly. For the synthesis of LMO–LNMO I, 17.5 mmol of MnO_2–S, 2.5 mmol of $Ni(NO_3)_2\cdot 6H_2O$, and 10.8 mmol of $LiNO_3$ were dispersed into 20 ml ethanol, and the following procedures were the same as those used for LNMO. In the synthesis of LMO, 20 mmol of MnO_2–S and 10.8 mmol of $LiNO_3$ were dispersed into 20 ml ethanol, and the following procedures were just like those used for LNMO. The LMO–LNMO mixture (LMO–LNMO M) was prepared by mixing equimolar amounts of LMO and LNMO by mechanical grinding.

2.2. Material characterization

The XRD patterns were collected on a Rigaku miniflex 600 instrument with Cu Kα radiation operating at 40 kV and 15 mA from 10° to 90° at 1° min^{-1} with a step size of 0.02°. The morphologies of the samples were characterized by field emission scanning electron microscopy (SEM, HITACHI S-4800), and energy dispersive X-ray spectroscopy (EDS, OXFORD 7426) was carried out for elemental analysis. Transmission electron microscopy (TEM, JEOL-2100) was further used to observe the morphology and identify the structure of the as-prepared samples. Raman spectra (JOBIN Yvon Horiba Raman Spectrometer model HR800) were collected with a 10 mW helium/neon laser at 532 nm excitation. The DSC/TG (STA 449 F3 Jupiter Netzsch) was used to measure the thermal stability of the electrodes in 1 M $LiPF_6$ salt dissolved in ethylene carbonate (EC) and dimethyl carbonate (DMC) with a mass ratio of 1 : 1 (#301 electrolyte, Guotai Huarong, China) from 100 °C to 300 °C at a heating rate of 5 °C min^{-1}. The detailed measurements were as follows. Firstly, a button cell was charged to a target state, then the cell was taken apart to get the electrode material film in an Ar-filled glove box. Secondly, the film was washed several times by DMC and naturally dried. Thirdly, the electrode materials scraped from the film and the electrolyte were sealed together in a gold-plated stainless steel crucible in the glove box. The ratio of electrolyte to electrode materials was 1 μL of electrolyte per milligram of electrode materials.

2.3. Electrochemical measurements

Electrochemical performances of these materials were evaluated in a CR2016-type coin-cell configuration. The cathode electrode film was obtained by spreading a slurry (70 wt% active material, 20 wt% acetylene black, 10 wt% polyvinylidene difluoride (PVDF) binder, dispersed in *N*-methyl pyrrolidone (NMP) solvent) onto an aluminum foil using a high-precision coating machine. After drying in a vacuum oven at 100 °C overnight, the electrode was punched out and roll-pressed. The coin cells were assembled by sandwiching a porous polyethylene separator between the electrode and Li metal foil in an Ar-filled glove box. The electrolyte used was a typical #301 electrolyte. The mass loading for all the cells was controlled to be about 3 mg cm^{-2}.

The cells were galvanostatically charged and discharged on a battery test system (LAND CT-2001A instrument, Wuhan, China) in the voltage range of 3.0–4.9 V at room temperature. When the rates were higher than 1 C (including 1 C), in order to overcome the polarization of the battery at high rates, a two-step charge process (constant current and constant voltage charge) was employed.[28] The specific capacity was calculated based on the total mass weight of LNMO and LMO in the electrode. The current values of various rates were calculated according to the theoretical capacity of LNMO. Take 1 C as an example, the current density value was 147 mA g^{-1}. Cyclic voltammogram (CV) measurements were performed on a CHI 660D potentiostat (Chenghua, Shanghai, China) at a scan rate of 0.1 mV s^{-1} in a potential range of 3.1 to 5.0 V. Electrochemical impedance spectra (EIS) were recorded on a Solartron SI 1287 electrochemical workstation with the frequency from 0.1 Hz to 100 kHz. All the tests were conducted at 25 °C unless specified otherwise.

3. Results and discussion

Fig. 1(a)–(e) show the SEM images of manganese sources of MnO_2–S, LMO, LNMO, LMO–LNMO M and LMO–LNMO I, respectively. Our starting precursor of the Mn source, microstructured MnO_2 spheres, is quite uniform, ranging from 2 μm to 4 μm in size. Each of these MnO_2 spheres is composed of many MnO_2 nano-needles radiating from its center, rendering the whole structure like a chestnut cupule. The nano-needles are well separated, with a large space between adjacent nanorods (Fig. S1†), generating a much larger surface area. Thus it is a better candidate for impregnation of solutions containing other transition metal ions. After calcination at 800 °C, the morphology of the spherical structure is retained and the particle size is in the range of 2–4 μm (Fig. 1(c)–(e)). From the high-magnification SEM image of LMO–LNMO I shown in Fig. 1(f), it can be concluded that microspheres are further made up by nano-octahedra, with each octahedron cross-linked by vertices or edges. Therefore, this special porous structure provides space for the infiltration of the electrolyte and accommodation for the volume change to alleviate the lattice strain during the insertion–deinsertion course of lithium ions.[29,30] The SEM study does not show a structural difference between LMO–LNMO M and LMO–LNMO I, but EDS elemental analysis presented in Fig. 2 clearly illustrates the difference. Fig. 2(a) shows the mapping area of LMO–LNMO M and Fig. 2(b) and (c) show the nickel and manganese elemental distributions from EDS of the selected area of LMO–LNMO M, respectively. The nickel distribution in this sample is not as homogeneous as that of manganese, and it does not exhibit overlapping as that of manganese, which is understandable since the two components were just mechanically mixed. Fig. 2(d)–(f) show the LMO–LNMO I sample. The distributions of Mn and Ni are not only very uniform, but also exhibit overlapping. This demonstrates unambiguously that LMO and LNMO both formed a homogeneous material at a nanoscale together rather than being simply blended.

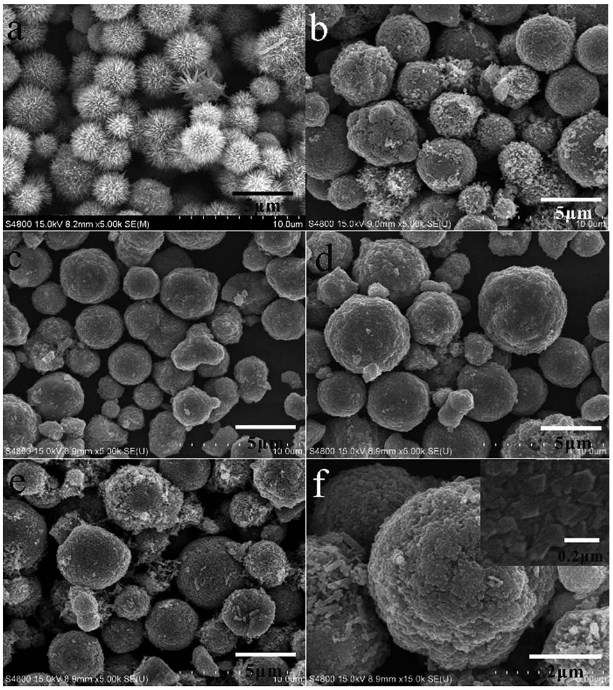

Fig. 1 SEM images of the samples (a) chestnut-like MnO_2, (b) LMO, (c) LNMO, (d) LMO–LNMO M, and (e) LMO–LNMO intergrowth. (f) A magnified image of LMO–LNMO I.

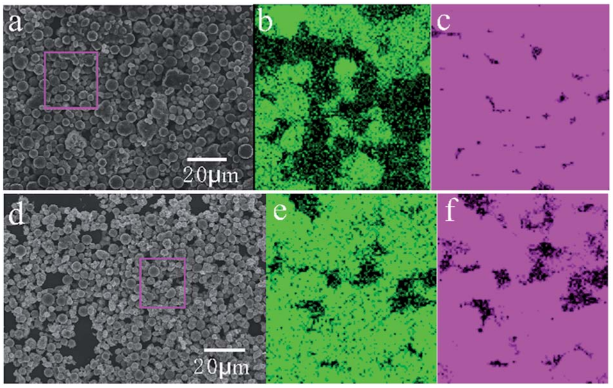

Fig. 2 (a) SEM plots of LMO–LNMO M, (b and c) EDS area maps of Ni, Mn element in the corresponding region (purple box) in SEM plots of LNMO–LMO M; (d) SEM plots of LMO–LNMO I, (e and f) EDS area maps of Ni and Mn elements in the corresponding region (purple box) in SEM plots of LNMO–LMO I.

Fig. 3 shows the X-ray diffraction (XRD) patterns of the LMO, LNMO, LMO–LNMO M and LMO–LNMO I, respectively. All these samples are indexed to cubic spinel structures. There are several weak peaks ($2\theta = 37.335°$, 43.381° and 63.024° (ref. 31)) in the LNMO which are from the rock salt phase $Li_xNi_{1-x}O$/NiO. The LMO–LNMO M is a simple mixture of LMO and the LNMO, thus, several pairs of twin peaks at *ca.* 38, 44, 48.3, 58.3, 64.0, 67.6, 76.0, 77.0, 81.0 and 84.0° are observed. In the LMO–LNMO I, no splitting of any peak is observed, indicating that it is a single phase material. The lattice parameters, $d_{(111)}$ and the size of sub-grains calculated using the Scherrer equation along the (111) surface are obtained from least square refinement based on a cubic structure using the PDXL2 software (Rigaku, Japan), and the results are summarized in Table 1. As we can see from the table, the crystal lattice parameters and interlayer space of the (111) lattice plane for LMO are 8.2342 Å and 4.7644 Å, respectively, while for LNMO they are 8.1690 Å and 4.7224 Å. The corresponding lattice parameters of LMO–LNMO I are in between that of the LMO and LNMO. To put it simply, with the

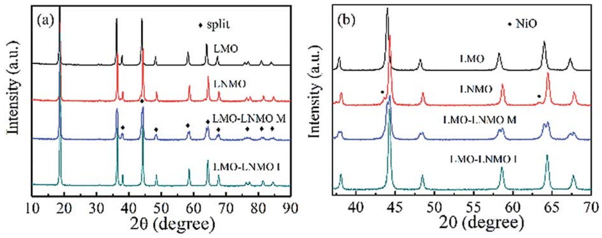

Fig. 3 XRD patterns of (a) LMO, LNMO, LMO–LNMO M and LMO–LNMO I; (b) enlargement of $2\theta = 37$ to 70° range.

Table 1 Summary of the lattice parameters for all the samples (a, b, c; $a = b = c$), $d_{(111)}$ and sizes of sub-grains

	Lattice parameter (Å)	$d_{(111)}$ (Å)	Sub-grain size (111) (Å)
LMO	8.2342	4.7644	410.16
LNMO	8.1690	4.7224	369.24
LMO–LNMO I	8.1834	4.7299	379.49

increase in the Ni content, the lattice parameter and interlayer space of (111) shrink. On the basis of the literature, this decrease is ascribed to the increase in the concentration of Mn^{4+} ions in the spinel structure because Mn^{3+} ions are replaced by Ni^{2+} ions.[32] Since the percentage of the Ni element in the LNMO is greater than that in LMO–LNMO I, its lattice and interlayer space of (111) are the smallest. The sub-grain sizes (Å) of the LMO, the LNMO and the LMO–LNMO I are 410.16 Å, 369.24 Å and 379.49 Å, which is in accordance with the lattice parameter.

The TEM characterization of the LMO–LNMO I is carried out (Fig. 4). As shown in Fig. 4(a), the LMO–LNMO I has a hollow structure, consistent with the structure of the precursor. The SAED pattern (Fig. 4(a) inset) of the whole micron-sized LMO–LNMO I sphere shows unordered diffraction spots, presenting the polycrystalline structure of the entire LMO–LNMO I sphere. The nano-sized polyhedron in Fig. 4(b) is obtained by magnifying the micron-sized LMO–LNMO I sphere surface. A high-resolution TEM (HRTEM) image of the nano-sized polyhedron of Fig. 4(b) shows clear lattice fringes (Fig. 4(c)). The interplanar spacing lattice is 0.48 nm, which is in accordance with the d-spacing of the (111) crystal planes of the LMO–LNMO I. The SAED pattern (Fig. 4(d)) with the electron beam in the [110] direction corresponding to the yellow area of Fig. 4(b) presents a well-organized array of diffraction spots that are indexed to a typical spinel lattice structure. This means that the polycrystalline LMO–LNMO I micron-sized sphere is composed of monocrystalline nano-sized polyhedra; LMO and LNMO in LMO–LNMO I both formed a homogeneous material at the unit cell scale. The ordered lattices in long-range order result in the easy intercalation and deintercalation of Li ions, which is useful to improve the rate properties of the cell with the material.

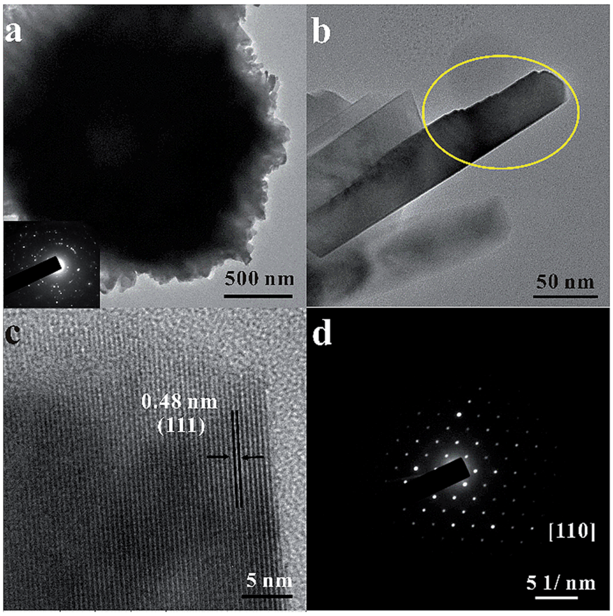

Fig. 4 TEM images of (a) the as-prepared LMO–LNMO I and (b) nano-sized polyhedra obtained by magnifying the LMO–LNMO I sphere surface. (c) HRTEM image of the nano-sized polyhedron and (d) SAED pattern in the [110] zone of the nano-sized polyhedron corresponding to the yellow area of (b).

Raman characterization was carried out as shown in Fig. 5 to identify the structure of the spinel. According to previous reports,[33,34] the strong band appearing at 623 cm^{-1} is attributed to the symmetrical Mn–O stretching vibration (A_{1g}) in MnO_6 octahedra. Peaks at around 388 and 481 cm^{-1} are related to the Ni^{2+}–O stretching mode in the spinel. The $T_{2g}^{(3)}$ band of the spinel is at around 575–625 cm^{-1}. The split of this $T_{2g}^{(3)}$ band is the fingerprint of the $P4_332$ space group. The splitting of $T_{2g}^{(3)}$ is weak and a broad hump is observed. The other characteristic peaks of the $P4_332$ structure around 212 and 157 cm^{-1} are weak with the absence of some characteristic peaks.[8,35] All these mean that LNMO is a mixture of orderly $P4_332$ and disorderly $Fd3m$ phases after annealing at 600 °C for 20 h. According to Patoux,[36] in general synthesis, the LNMO is usually a mixture of an ordered $P4_332$ phase and a disordered $Fd3m$ phase. The peaks of LMO–LNMO I are similar to those of LNMO with little shift of the peak position. So the orderly and disorderly sites of Ni and Mn in LMO–LNMO I coexist.

Cyclic voltammograms of LMO, LNMO, LMO–LNMO M and LMO–LNMO I at a scanning rate of 0.1 mV s^{-1} are shown in Fig. 6. In general, the redox peaks at around 4.1 V are ascribed to oxidation/reduction of Mn^{4+}/Mn^{3+}, while the one at 4.7 V is attributed to the redox reaction of the Ni^{4+}/Ni^{2+} couples. The peaks of LMO–LNMO M are simple additions of those of LMO and LNMO with neither shifting the peak positions nor changing their relative intensities. The LMO–LNMO I exhibits distinct differences. The peak intensity in the range of 4.0–4.3 V becomes relatively smaller and broader.

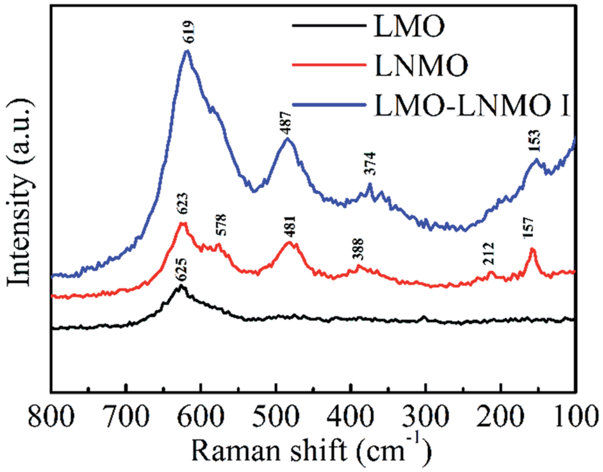

Fig. 5 Raman spectra of LMO, LNMO and LMO–LNMO I.

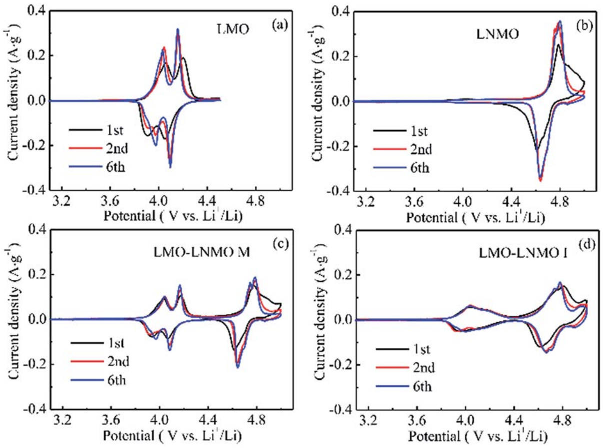

Fig. 6 Cyclic voltammogram curves (at a scan rate of 0.1 mV s^{-1}) of (a) LMO, (b) LNMO, (c) LMO–LNMO M, and (d) LMO–LNMO I.

The electrochemical performances of these materials at 25 °C are given in Fig. 7. Fig. 7(c) plots their specific discharge capacities upon cycling at 1 C. The discharge capacities (here we used the fifth cycle at which their discharge capacities were stabilized) of LMO, LNMO, LMO–LNMO M, and LMO–LNMO I are 111.7, 117.7, 119.7 and 128.8 mA h g^{-1}, respectively. After 100 cycles, their specific capacities became 105.1, 113.5, 111.5 and 124.8 mA h g^{-1}, with specific capacity retentions of 94.1%, 96.4%, 93.2% and 96.9%, respectively. Although the content of LMO in the LMO–LNMO M is up to 50% compared to LNMO and LMO, their discharge specific capacities and cycle performances are essentially the same as LNMO and better than LMO, suggesting that a simple blending improves the electrochemical performance of the material to some extent. The LMO–LNMO I, which has a better mixing of Mn and Ni ions, not only showed roughly 10% discharge capacity increase, but also the highest capacity retention. We believe that in LMO–LNMO I, LNMO is an active material as well as a skeleton for the LMO, so that more lithium ions can take part in the insertion–deinsertion process. The charge and discharge-capacity/voltage curves of the fifth cycle are plotted in Fig. 7(a) and (b). These data are consistent with the CV plots shown in Fig. 6. Two plateaus around 4.1 V were observed for LMO, one plateau at 4.7 V for LNMO. The discharge plateaus for the LMO–LNMO M are simple additions of LMO and LNMO. The LMO–LNMO I also showed a similar voltage plateau to LMO–LNMO M, but significant differences are observable: the discharge plateau around 4.7 V becomes larger, and the discharge plateau around 4.1 V rises to higher voltage (4.2 V). Because the platform of LMO is located at 4.1 V, so in the charge test of LMO, the cutoff voltage is set to 4.3 V. We also did the electrochemical test of LMO in the voltage range of 3.0–4.9 V as in Fig. S2.† It was found that there is a little increase in the discharge capacity for LMO, but it is still less than that of LMO–LNMO I.

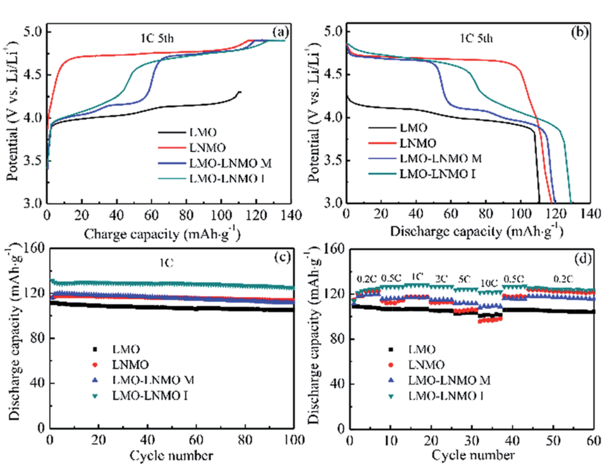

Fig. 7 Electrochemical properties of the as-prepared samples (a) the 5th charge curve at 1 C; (b) the 5th discharge curve at 1 C; (c) cycle performance at 1 C; and (d) rate cycling performance.

The rate capabilities of these materials are shown in Fig. 7(d). Because of the electrochemical polarization and ohmic polarization from the restricted diffusion rate of lithium ions in the spinel structure,[37] the capacity of all the samples certainly reduces at high rates. Among all these samples, LNMO showed the largest reduction in capacity at high rates, LMO–LNMO M followed LNMO, and LMO–LNMO I showed the least reduction in capacity at the same high rates, which is due to the homogeneous mixing of Ni and Mn ions in the structure. Ni ions act as structural stabilization agents to make excess lithium ions engage in the charge–discharge process; Mn ions boost the electrical conductivity of the material by making Ni sites and Mn sites more homogeneous,[25] leading to greater specific capacity at high rates. Strikingly, the discharge capacity at 1 C for the LMO–LNMO I was even higher than that at 0.5 C. Such a phenomenon has been reported by Zhou[28] and Lazarraga[38] without a clear conclusion. In our opinion, this may be due to the different charging modes between 0.5 C and 1 C. In our experiment, the cells were galvanostatically charged and discharged on a battery test system between 3.0 and 4.9 V at room temperature at low rates. When the rates were higher than 1 C (including 1 C), a two-step charge process (constant current and constant voltage charge) was employed in order to overcome the polarization of the battery at high rates. In the latter case, following the constant current charge step, the constant voltage charge process was carried out till the current reduced to one tenth of its initial constant value.

Fig. 8 shows typical cycle performances of the electrodes at a current rate of 5 C between 3.0 and 5.0 V at 55 °C. The discharge capacity of LMO, LNMO, LMO–LNMO M, LMO–LNMO I at the fifth cycle is 108.1, 116.3, 116.6 and 130.6 mA h g^{-1}, with a retention of 93.2%, 90.1%, 91% and 93.7% after 120 cycles, respectively. The charge platform of the LMO–LNMO I is lower than that of the LMO–LNMO M, whereas the discharge platform is higher than that of the LMO–LNMO M, indicating less ohmic polarization.[37] The LMO–LNMO M charge–discharge curves can be regarded as the simple summation of LMO and LNMO. All these suggest that Ni and Mn ions in LMO–LNMO I achieve homogeneous mixing at the atomic level, making the structure more stable than LMO–LNMO M.

The electrochemical impedance spectroscopy (EIS) test was conducted to further illustrate the differences in the

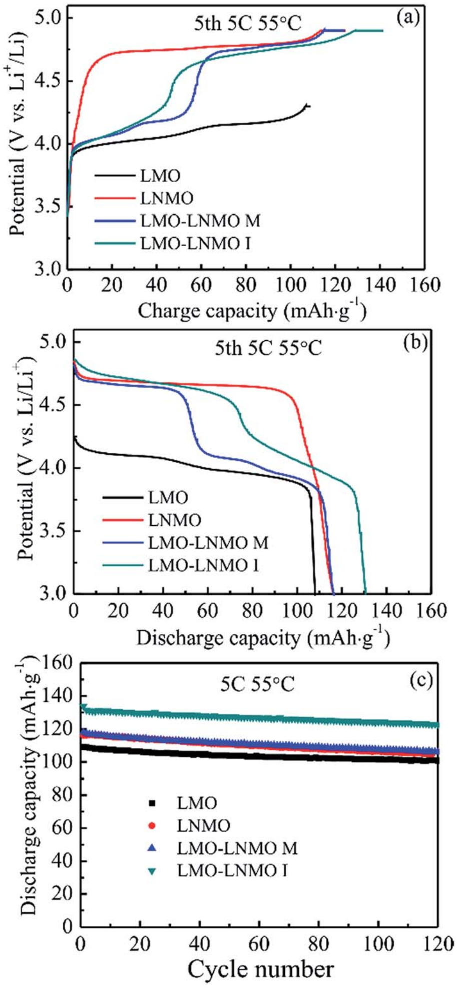

Fig. 8 Electrochemical properties of the samples at 55 °C at 5 C: (a) the fifth charge curve, (b) the fifth discharge curve, and (c) the cycle performance of samples.

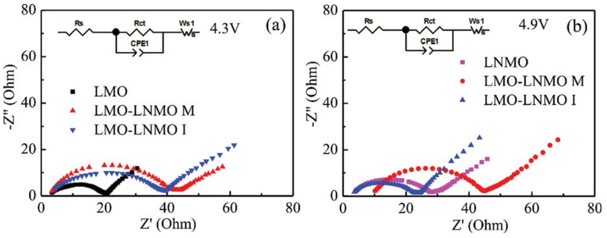

Fig. 9 EIS spectra of the samples in the frequency range between 0.1 Hz and 100 kHz at 25 °C: (a) charged to 4.3 V, (b) charged to 4.9 V.

Table 2 The fitted results of resistances (R_s) and charge transfer resistances (R_{ct}) for the Nyquist plots of the LMO, the LNMO, the LNMO–LMO M, and the LNMO–LMO I samples at the charged states of 4.3 V and 4.9 V

	Charge to 4.3 V (Ω)		Charge to 4.9 V (Ω)	
	R_s	R_{ct}	R_s	R_{ct}
LMO	2.23	17.82		
LNMO			2.30	25.49
LMO–LNMO M	2.47	38.39	9.29	35.83
LMO–LNMO I	2.03	35.86	2.11	21.09

electrochemical polarization and ohmic polarization. All the samples were charged and discharged at 1 C by a constant current and constant voltage process. After four full cycles, the cells were charged to 4.3 V, then EIS was performed in the range of 100 kHz to 0.1 Hz. The EIS of the 4.9 V charged state was performed similar to the above except that cells were charged to 4.9 V at 1 C, then the potential was kept at 4.9 V until the current decreases to one tenth of its initial value. The Nyquist plots (Fig. 9(a)) of all materials charged to 4.3 V display similar profiles: a semicircle in the high-frequency region and a linear slope in the low-frequency region. All can be fitted with the same equivalent circuits as shown in the insets of Fig. 9(a). When the materials were charged to 4.9 V, similar Nyquist plots and equivalent circuits were obtained. The fitted data are listed in Table 2. In our analysis, R_s is assigned to the electrolyte resistance, while R_{ct} is attributed to the direct charge transfer resistance of electrode materials.[39–41] The R_{ct} of LNMO, LMO–LNMO M and LMO–LNMO I (<40 Ω) varies substantially, $R_{ct_{LMO-LNMO\ M}} > R_{ct_{LMO-LNMO\ I}} > R_{ct_{LMO}}$ at the 4.3 V charged state and $R_{ct_{LMO-LNMO\ M}} > R_{ct_{LNMO}} > R_{ct_{LMO-LNMO\ I}}$ at the 4.9 V charged state in sequential order. This indicates that the intergrown LMO–LNMO I reduces the barrier for the electron transfer at the electrode–electrolyte interface. The much improved rate performance from the decreasing R_{ct} of LMO–LNMO I is attributed to its unique structure. Because of the homogeneous mixing of Ni and Mn ions at the atomic level in the LMO–LNMO I, the structure became more stable and highly electrically conductive,[42] thus facilitating the insertion–deinsertion of lithium ions by the alleviation of electrochemical polarization and ohmic polarization. The R_{ct} of LMO–LNMO M is a little higher than that of LNMO, which may be attributed to the two phase structure of LMO–LNMO M. This is a little unfavourable to lithium ion transport.

The thermal behaviors of charged (delithiated, 4.3 V and 4.9 V) LNMO–LMO I and blend LNMO–LMO M in 301 electrolyte (1 M $LiPF_6$, EC/DMC) were investigated by DSC/TG analysis as shown in Fig. 10. Pure $LiMn_2O_4$ and $LiNi_{0.5}Mn_{1.5}O_4$ spinel were also evaluated for comparison. There are obvious differences in thermostability among LMO, LNMO, LMO–LNMO M and LMO–LNMO I. As the battery was charged to 4.3 V (Fig. 10(a)), the onset exothermic temperature for LMO is 159.4 °C, while that of LMO–LNMO M is 171.3 °C. The thermostability is boosted by the mixture of LMO and LNMO, but this is also inferior to LMO–LNMO I. Due to the Ni and Mn mingling at the atomic level, the onset exothermic temperature at the 4.3 V state is back to 188.1 °C. The total heat quantity for LMO around 160–300 °C is 599.9 J g^{-1}, while that for LMO–LNMO I is 567.1 J g^{-1}. When the thermal stability was measured at the fully delithiated state (4.9 V), the onset exothermic temperature for LMO–LNMO M is higher than that for LNMO and LMO–LNMO I, which may be attributed to a blend effect. As per Tran's research,[43] after

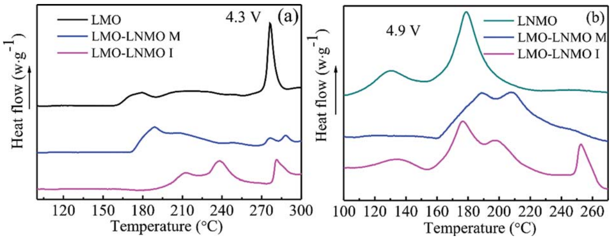

Fig. 10 DSC curves of samples in #301 electrolyte at the states charged to 4.3 V (a), and to 4.9 V (b).

blending 33.3% $LiNi_{0.8}Co_{0.15}Al_{0.05}O_2$ and 66.7% $LiMn_2O_4$, the thermal stability of the blending material is improved tremendously compared to that of $LiNi_{0.8}Co_{0.15}Al_{0.05}O_2$ and $LiMn_2O_4$ monomers. The LNMO–LMO I has a little lower onset exothermic temperature, but has the lowest reaction heat flow of 518.9 J g^{-1} in the temperature range of 100–280 °C. For LNMO–LMO M and LNMO, the reaction heat flow is nearly the same, 698.6 J g^{-1} and 689.6 J g^{-1}, respectively. These results suggest that LNMO–LMO I has a stable structure compared to LMO, LNMO and LNMO–LMO M.

4. Conclusion

In this work, the porous micron-sized spheres of intergrown LMO–LNMO I particles are successfully synthesized *via* an impregnation method based on highly reactive chestnut-like MnO_2 spheres as the manganese sources and structural templates. The LMO–LNMO I is composed of a nano-sized octahedron with good crystallinity with particle size ranging from 2–4 μm. In this special structure, the LNMO works as a skeleton to stabilize the structure of LMO, ensuring that more lithium ions in LMO participate in the charge–discharge process along with those in LNMO. As a result, LMO–LNMO presents a discharge specific capacity of 130 mA h g at 1 C at 25 °C, with a capacity retention of 96.2% after 100 cycles. It also shows an excellent performance at high temperature and high rate. It can deliver a discharge capacity of 131 mA h g^{-1}, with a capacity retention of 95% after 100 cycles at 5 C at 55 °C. Meanwhile, with the improved Mn content and better Ni/Mn ion mixing in the LMO–LNMO I compared to those in LNMO and LMO–LNMO M, the thermostability of LNMO–LMO I is much improved compared with that of LNMO. The high capacity, excellent rate capability, and remarkable cycling stability of the LMO–LNMO I at room and elevated temperature make it a promising cathode material for lithium ion batteries.

Acknowledgements

The authors gratefully acknowledge the financial support from the National High Technology Research and Development Program of China (2012AA110204), Key Project of Science and Technology of Fujian Province (2013H6022), Science and Technology Bureau of Xiamen (Grant No. 3502Z20133004) and National Natural Science Foundation of China (21321062). Jiyang Li expresses their special thanks to National Fund for Fostering Talents of Basic Science (J1310024). The authors also wish to express their thanks to Drs Dong Sun, Binbin Xu and Chuan Liu for their valuable suggestions.

Notes and references

1 D. Liu, J. Trottier, P. Charest, J. Fréchette, A. Guerfi, A. Mauger, C. M. Julien and K. Zaghib, *J. Power Sources*, 2012, **204**, 127–132.
2 S. Yang, J. Chen, Y. Liu and B. Yi, *J. Mater. Chem. A*, 2014, **2**, 9322–9330.
3 J. Yang, F. Cheng, X. Zhang, H. Gao, Z. Tao and J. Chen, *J. Mater. Chem. A*, 2014, **2**, 1636–1640.
4 X. Wu, S. Wang, X. Lin, G. Zhong, Z. Gong and Y. Yang, *J. Mater. Chem. A*, 2014, **2**, 1006–1013.
5 J. Wang, W. Lin, B. Wu and J. Zhao, *Electrochim. Acta*, 2014, **145**, 245–253.
6 Z. Yang, J. Zhang, M. C. W. Kintner-Meyer, X. Lu, D. Choi, J. P. Lemmon and J. Liu, *Chem. Rev.*, 2011, **111**, 3577–3613.
7 J. Wang, W. Lin, B. Wu and J. Zhao, *J. Mater. Chem. A*, 2014, **2**, 16434–16442.
8 G. B. Zhong, Y. Y. Wang, X. J. Zhao, Q. S. Wang, Y. Yu and C. H. Chen, *J. Power Sources*, 2012, **216**, 368–375.
9 G. N. Zhu, L. Chen, Y. G. Wang, C. X. Wang, R. C. Che and Y. Y. Xia, *Adv. Funct. Mater.*, 2013, **23**, 640–647.
10 Y. L. Ding, J. Xie, G. S. Cao, T. J. Zhu, H. M. Yu and X. B. Zhao, *Adv. Funct. Mater.*, 2011, **21**, 348–355.
11 M. J. Lee, S. Lee, P. Oh, Y. Kim and J. Cho, *Nano Lett.*, 2014, **14**, 993–999.
12 D. Tang, Y. Sun, Z. Yang, L. Ben, L. Gu and X. Huang, *Chem. Mater.*, 2014, **26**, 3535–3543.
13 Y. Koyama, H. Arai, I. Tanaka, Y. Uchimoto and Z. Ogumi, *J. Mater. Chem. A*, 2014, **2**, 11235–11245.
14 H. M. Cheng, F. M. Wang, J. P. Chu, R. Santhanam, J. Rick and S. C. Lo, *J. Phys. Chem. C*, 2012, **116**, 7629–7637.
15 S. Lee, Y. Cho, H. K. Song, K. T. Lee and J. Cho, *Angew. Chem.*, 2012, **124**, 8878–8882.
16 T. F. Yi, Y. Xie, Y. R. Zhu, R. S. Zhu and M. F. Ye, *J. Power Sources*, 2012, **211**, 59–65.
17 H. W. Lee, P. Muralidharan, R. Ruffo, C. M. Mari, Y. Cui and D. K. Kim, *Nano Lett.*, 2010, **10**, 3852–3856.
18 Y. Wu, Z. Wen, H. Feng and J. Li, *Small*, 2012, **8**, 858–862.
19 S. Brutti, G. Greco, P. Reale and S. Panero, *Electrochim. Acta*, 2013, **106**, 483–493.
20 J.-H. Kim, N. P. W. Pieczonka, Z. Li, Y. Wu, S. Harris and B. R. Powell, *Electrochim. Acta*, 2013, **90**, 556–562.
21 Y. J. Wei, L. Y. Yan, C. Z. Wang, X. G. Xu, F. Wu and G. Chen, *J. Phys. Chem. B*, 2004, **108**, 18547–18551.
22 S. Mandal, R. M. Rojas, J. M. Amarilla, P. Calle, N. V. Kosova, V. F. Anufrienko and J. M. Rojo, *Chem. Mater.*, 2002, **14**, 1598–1605.
23 Y. L. Ding, J. Xie, G. S. Cao, T. J. Zhu, H. M. Yu and X. B. Zhao, *J. Phys. Chem. C*, 2011, **115**, 9821–9825.
24 S. Wang, J. Yang, X. Wu, Y. Li, Z. Gong, W. Wen, M. Lin, J. Yang and Y. Yang, *J. Power Sources*, 2014, **245**, 570–578.
25 J. Xiao, X. Chen, P. V. Sushko, M. L. Sushko, L. Kovarik, J. Feng, Z. Deng, J. Zheng, G. L. Graff, Z. Nie, D. Choi,

J. Liu, J.-G. Zhang and M. S. Whittingham, *Adv. Mater.*, 2012, **24**, 2109–2116.
26 H. E. Wang and D. Qian, *Mater. Chem. Phys.*, 2008, **109**, 399–403.
27 X. Zhu, X. Li, Y. Zhu, S. Jin, Y. Wang and Y. Qian, *Electrochim. Acta*, 2014, **121**, 253–257.
28 L. Zhou, D. Zhao and X. Lou, *Angew. Chem.*, 2012, **124**, 243–245.
29 S. Liang, J. Yi and A. Pan, *Int. J. Electrochem. Sci.*, 2013, **8**, 6535–6543.
30 X. W. Lou, L. A. Archer and Z. Yang, *Adv. Mater.*, 2008, **20**, 3987–4019.
31 J. Song, D. W. Shin, Y. Lu, C. D. Amos, A. Manthiram and J. B. Goodenough, *Chem. Mater.*, 2012, **24**, 3101–3109.
32 Q. Zhong, A. Bonakdarpour, M. Zhang, Y. Gao and J. R. Dahn, *J. Electrochem. Soc.*, 1997, **144**, 205–213.
33 C. M. Julien and M. Massot, *Mater. Sci. Eng., B*, 2003, **97**, 217–230.
34 S. H. Oh, K. Y. Chung, S. H. Jeon, C. S. Kim, W. I. Cho and B. W. Cho, *J. Alloys Compd.*, 2009, **469**, 244–250.
35 G. B. Zhong, Y. Y. Wang, Y. Q. Yu and C. H. Chen, *J. Power Sources*, 2012, **205**, 385–393.
36 S. Patoux, L. Daniel, C. Bourbon, H. Lignier, C. Pagano, F. Le Cras, S. Jouanneau and S. Martinet, *J. Power Sources*, 2009, **189**, 344–352.
37 O. Sha, Z. Tang, S. Wang, W. Yuan, Z. Qiao, Q. Xu and L. Ma, *Electrochim. Acta*, 2012, **77**, 250–255.
38 M. G. Lazarraga, L. Pascual, H. Gadjov, D. Kovacheva, K. Petrov, J. M. Amarilla, R. M. Rojas, M. A. Martin-Luengo and J. M. Rojo, *J. Mater. Chem.*, 2004, **14**, 1640–1647.
39 L. J. Xi, H. E. Wang, Z. G. Lu, S. L. Yang, R. G. Ma, J. Q. Deng and C. Y. Chung, *J. Power Sources*, 2012, **198**, 251–257.
40 J. Chong, S. Xun, X. Song, G. Liu and V. S. Battaglia, *Nano Energy*, 2013, **2**, 283–293.
41 J. Lu, Q. Peng, W. Wang, C. Nan, L. Li and Y. Li, *J. Am. Chem. Soc.*, 2013, **135**, 1649–1652.
42 M. Kunduraci, J. F. Al-Sharab and G. G. Amatucci, *Chem. Mater.*, 2006, **18**, 3585–3592.
43 H. Y. Tran, C. Täubert, M. Fleischhammer, P. Axmann, L. Küppers and M. Wohlfahrt-Mehrens, *J. Electrochem. Soc.*, 2011, **158**, A556–A561.